Chemical Science

ROYAL SOCIETY OF CHEMISTRY

EDGE ARTICLE

View Article Online
View Journal | View Issue

Cite this: *Chem. Sci.*, 2023, **14**, 1205

All publication charges for this article have been paid for by the Royal Society of Chemistry

Branching phenomena in nanostructure synthesis illuminated by the study of Ni-based nanocomposites†

Liang Qiao, ‡[abc] Zheng Fu,‡[ad] Wenxia Zhao,[ae] Yan Cui,[b] Xin Xing,[b] Yin Xie,[b] Ji Li,[af] Guanhui Gao,[g] Zhengxi Xuan,[ad] Yang Liu,[a] Chaeeon Lee,[a] Yimo Han,[g] Yingwen Cheng,[h] Shengbao He,*[b] Matthew R. Jones *[cg] and Mark T. Swihart *[ad]

Received 11th September 2022
Accepted 25th December 2022

DOI: 10.1039/d2sc05077c

rsc.li/chemical-science

Branching phenomena are ubiquitous in both natural and artificial crystallization processes. The branched nanostructures' emergent properties depend upon their structures, but their structural tunability is limited by an inadequate understanding of their formation mechanisms. Here we developed an ensemble of Nickel-Based nano-Composites (NBCs) to investigate branching phenomena in solution-phase synthesis with precision and in depth. NBCs of 24 morphologies, including dots, core@shell dots, hollow shells, clusters, polyhedra, platelets, dendrites, urchins, and dandelions, were synthesized through systematic adjustment of multiple synthesis parameters. Relationships between the synthesis parameters and the resultant morphologies were analyzed. Classical or non-classical models of nucleation, nascent growth, 1D growth, 2D growth, 3D reconstruction, aggregation, and carburization were defined individually and then integrated to provide a holistic view of the formation mechanism of branched NBCs. Finally, guidelines were extracted and verified to guide the rational solution-phase syntheses of branched nanomaterials with emergent biological, chemical, and physical properties for potential applications in immunology, catalysis, energy storage, and optics. Demonstrating a systematic approach for deconvoluting the formation mechanism and enhancing the synthesis tunability, this work is intended to benefit the conception, development, and improvement of analogous artificial branched nanostructures. Moreover, the progress on this front of synthesis science would, hopefully, deepen our understanding of branching phenomena in nature.

Introduction

Branching phenomena are ubiquitous in the growth of complex structures, both natural (*e.g.*, snowflakes),[1] and artificial (*e.g.*, Ni,[2] Ni_3C,[3] Al,[4] and Pd–Pt (ref. 5) nanoparticles (NPs)). Branched nanostructures are valuable in numerous applications, *e.g.*, for immunology, the branched microparticles can stimulate and enhance immune responses, *in vitro* and *in vivo*;[6] for catalysis, branched Ni_3C NPs efficiently catalyzed methanol electro-oxidation;[3] for energy storage, branched Ni NPs helped prevent thermal runaway in high-energy-density batteries;[7] for optics, polystyrene spheres with ZnO branches can disperse in both hydrophobic and hydrophilic media, and exhibit wide optical response.[8,9] All of these intriguing biological, chemical, and physical properties depend upon the nanostructures' branched morphologies, but the morphology control can only garner limited support from the current understanding of the branching mechanism.[10–14] Hence a deeper mechanistic understanding is called for. Specifically, the intrinsic complexity, *i.e.*, instability-induced symmetry breaking and non-equilibrium process-induced kinetic trapping, are not

[a]*Department of Chemical and Biological Engineering, University at Buffalo (SUNY), Buffalo, NY 14260, USA . E-mail: swihart@buffalo.edu*

[b]*Division of Fundamental Research, Petrochemical Research Institute, PetroChina, Beijing 102206, China. E-mail: hsb@petrochina.com.cn*

[c]*Department of Chemistry, Rice University, Houston, Texas 77005, USA. E-mail: mrj@rice.edu*

[d]*RENEW Institute, University at Buffalo (SUNY), Buffalo, New York 14260, USA*

[e]*School of Chemistry and Chemical Engineering, Ningxia Normal University, Guyuan 756000, China*

[f]*MIIT Key Laboratory of Critical Materials Technology for New Energy Conversion and Storage, School of Chemistry and Chemical Engineering, Harbin Institute of Technology, Harbin, Heilongjiang 150001, China*

[g]*Department of Materials Science and NanoEngineering, Rice University, Houston, Texas 77005, USA*

[h]*Department of Chemistry and Biochemistry, Northern Illinois University, DeKalb, Illinois 60115, USA*

† Electronic supplementary information (ESI) available: Fig. S1–S5 additional figures, including the size distributions (with additional TEM/SEM images), XRD patterns, contrast profiles, and FIB-SEM images (PDF). Table S1 the synthesis parameters of the NBCs (XLSX). See DOI: https://doi.org/10.1039/d2sc05077c

‡ L. Qiao and Z. Fu contributed equally to this work.

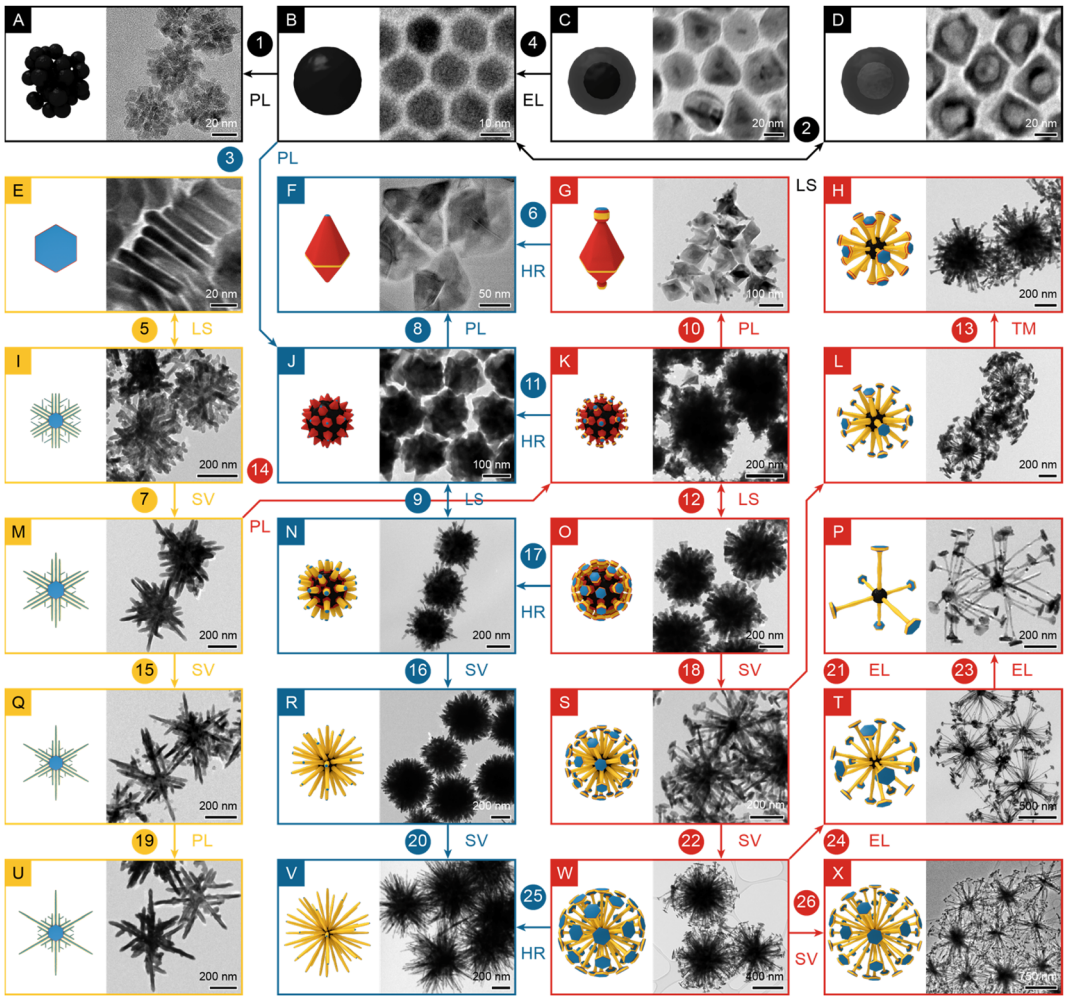

Fig. 1 The atlas of NBCs. (A) Clusters; (B) dots; (C) core@shell dots; (D) shells; (E) platelets; (F) polyhedra; (G) polyhedra with stubs; (H) dandelions with bulbs; (I, M, Q and U) dendrites; (J) polyhedral aggregates; (K) polyhedral aggregates with stubs; (N, R and V) urchins; (L, O, P, S, T, W and X) dandelions. 0D dots are labelled in black; 2D dendrites in yellow; 3D urchins in blue; 3D dandelions in red. Single and double arrows indicate the increase or switch of a parameter, respectively: TM, time; HR, heating rate; LS, ligand species; PL, promoting ligand concentration; EL, etching ligand concentration; SV, solvent volume.

sufficiently understood to predict the timing and extent of branching. Thus, a comprehensive study of a well-defined model system can lend valuable insights to advance our understanding of branching phenomena with precision and in depth.

To bridge this gap, investigated the branched Nickel-Based nano-Composites (NBCs). The ensemble of NBCs constituted a robust platform for studying the branching phenomena for three reasons. First, the branched NBCs can be high-performing catalysts,[2,3] catalyst substrates,[15] or battery materials,[7] so the developed nanostructures, as the subjects of mechanistic study, can also be of value in relevant applications. Second, NBCs, *e.g.*, Ni,[2] Ni_3C,[16] or Ni–Ni_3C,[17] tend to form branched nanostructures, but the intrinsic mechanism remains elusive. Third, the fully branched morphologies of the NBCs synthesized in solution phase can be autonomously locked by an isomorphic surface carburization process. As reported earlier,[18] the NBCs preliminarily formed as pure Ni NPs, and then over extended heating, the surface of the branched Ni NPs can be carburized to form a thin carbidic layer, which prevents further growth and constrains the morphological deformation of the Ni cores, so their complex morphologies could be preserved for post-processing and characterization. This locking mechanism is also demonstrated by the absence of carbidic layer between the components of the complex NBCs, *e.g.*, clusters (Fig. 1A and 2-d2), because if the carburization of the components occurred before their assembly, the components would have been separated by carbidic layers. In short, the NBCs were chosen as the platform because of their practical functions, elusive branching mechanism, and autonomous locking of the complex morphologies.

Here we aim to show that, with the synthesis and analysis of the ensemble of NBCs, a deeper understanding of the formation mechanism of branched nanostructures can be established to enhance the tunability of such syntheses. To achieve this goal, the report is structured as follows: NBCs of 24 diverse

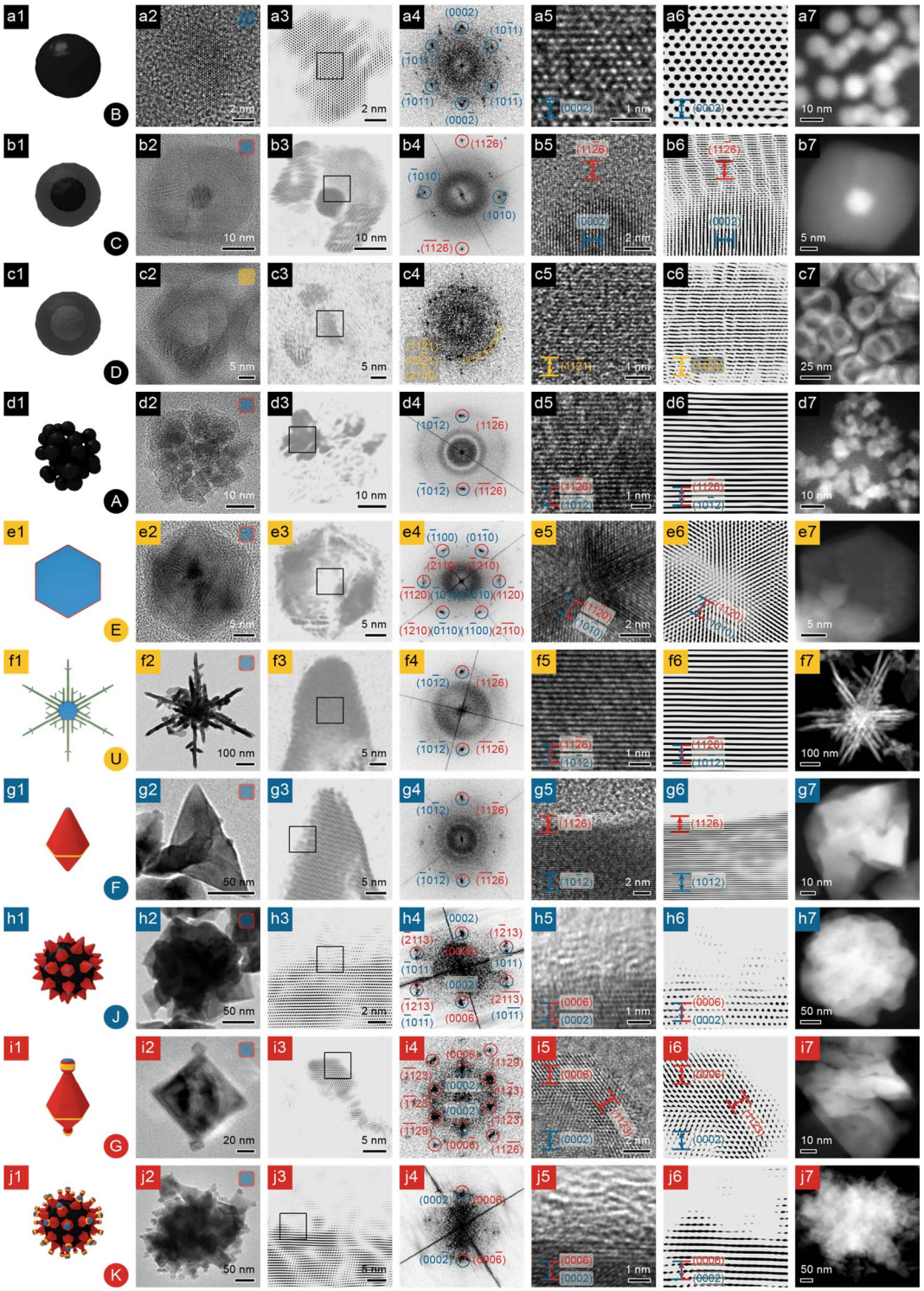

Fig. 2 Structural and compositional analyses of NBCs, part 1. (a) Dots; (b) core@shell dots; (c) shells; (d) clusters; (e) platelets; (f) dendrites; (g and h) polyhedra and their aggregates; (i and j) polyhedra with stubs and their aggregates. Column 1: 3D model (the inset at the lower right corner is the morphology's serial number from Fig. 1); column 2: TEM image (the inset at the upper right corner represents the chemical composition of the NBC: blue represents Ni; orange Ni_2P; red Ni_3C); column 3: FFT-filtered TEM image (the square indicates the region enlarged in column 5); column 4: indexed FFT pattern of the HRTEM image in column 5 (spots of Ni indexed in blue; Ni_3C in red); column 5: HRTEM image (facets of Ni labelled in blue; Ni_3C in red); column 6: FFT-filtered HRTEM image; column 7: HAADF STEM image. Scale bars are shared by column 5 and 6.

morphologies were prepared (Fig. 1); each NBC was inspected with a suite of complementary techniques for aquiring structural and compositional information (Fig. 2–4); the synthesis parameters' effects on the morphologies were analyzed to identify the key parameters; growth models for individual steps (Fig. 5), classical or non-classical, were defined based upon

fundamental thermodynamic and kinetic principles, and were then logically integrated to elucidate the holistic formation mechanism; finally, certain guidelines were extracted and verified to facilitate the solution-phase synthesis of branched nanostructures.

Results and discussion

Twenty-four NBCs of distinctive shapes (see the TEM images and illustrations in Fig. 1), the majority of which are of uniform size (see the size distributions in Fig. S1†), were prepared *via* solution-phase synthesis and categorized into four sets: 0D dots, 2D dendrites, 3D urchins, and 3D dandelions. 0D dots included four quasi-isotropic sub-30 nm NPs (Fig. 1A–D) that formed rapidly with low ligand concentration and fast heating rate ($\sim$5.26 °C min^{-1}). 2D dendrites included five plates/dendrites of up to $\sim$700 nm (Fig. 1E, I, M, Q and U) that were prepared with low ligand concentration and slow heating rate ($\sim$3.42 °C min^{-1}). 3D urchins included five NBCs of up to $\sim$800 nm (Fig. 1F, J, N, R and V) that were produced with high ligand concentration and fast heating rate ($\sim$5.26 °C min^{-1}). 3D dandelions, the most complex set, included ten NBCs of up to $\sim$1200 nm (Fig. 1G, H and below), which were synthesized with high ligand concentration and slow heating rate ($\sim$3.42 °C min^{-1}). Overall, these NBCs exhibited an array of diverse branched morphologies that were seemingly inexplicable by classic growth models.[19]

Morphological analysis

To study their branching mechanism, the morphologies and compositions of the NBCs must be unraveled with care, so X-Ray Diffraction (XRD), Scanning Electron Microscopy (SEM), High-Angle Annular Dark Field – Scanning Transmission Electron Microscopy (HAADF-STEM), and High-Resolution Transmission Electron Microscopy (HRTEM)) were performed and integrated to provide abundant and complementary structural and compositional evidence.

Dots (Fig. 1B). Dots are namely NPs without well-defined facets, as illustrated in Fig. 2-a1 and outlined in the HAADF image in Fig. 2-a7. In the HRTEM images, the dots appear to be single crystalline (Fig. 2-a2 and a3), and their *d*-spacing of $\sim$2.17 Å matched $(0002)_{Ni}$, as indicated by the blue arrows (Fig. 2-a5 and a6). In addition, the XRD pattern of the dots (Fig. S2a†) is an exact match to Hexagonal Close-Packed (HCP) Ni (PDF #45-1027, Fig. 4a), with peaks at 39.1°, 41.5°, and 44.5°. Hence, in this paper, the subscript Ni for the crystalline planes/directions stands for HCP Ni. Based on this evidence, the dots are identified as single crystalline, HCP Ni dots without defined facets.

Core@shell dots (Fig. 1C). The core@shell dots are of irregular shapes with a shell having contrast that is $\sim$50% of the contrast of the core, as illustrated in profiles shown in Fig. S3† (Fig. 1C, 2-b7 and S3a†). In the previously reported Ni@Ni_3C nanostructures, the polycrystalline Ni_3C shells have a lower contrast than the Ni cores,[18] which is consistent with our observation of the core@shell dots here (Fig. 2-b2 and b3). Moreover, according to the HRTEM images (Fig. 2-b5 and b6) and the corresponding Fast Fourier Transform (FFT) pattern (Fig. 2-b4), the *d*-spacing of the shell ($\sim$1.57 Å) matches $(11\bar{2}6)_{Ni_3C}$ (Ni_3C PDF #06-0697, Fig. 4b), and the *d*-spacing of the core ($\sim$2.17 Å) matches $(0002)_{Ni}$ (HCP Ni PDF #45-1027, Fig. 4a), confirming this core@shell NBC as HCP Ni core@rhombohedral Ni_3C shell.

Shells (Fig. 1D). These nanoshells of irregular shapes were highly polycrystalline, as revealed by the TEM image and the corresponding FFT pattern (Fig. 2-c2–c4). The HRTEM images in Fig. 2-c5 and c6 revealed that the *d*-spacing matched $(11\bar{2}1)_{Ni_2P}$. In addition, the Ni_2P phase (PDF #65-9706, Fig. 4c) has been observed as a prevalent phase during the previously reported Ni_2P syntheses.[20,21] Therefore, these nanostructures can be determined as polycrystalline Ni_2P nanoshells.

Clusters (Fig. 1A). These clusters appear as randomly-shaped aggregates of dots. However, each cluster is single crystalline (Fig. 2-d2–d4), suggesting the oriented attachment of individual dots into clusters, as previously reported for nanoclusters of branched shapes.[22] Similar to the core@shell dots (Fig. 1C), each cluster as a whole is covered in a thin layer of Ni_3C, but the constituent Ni NPs do not have a lighter Ni_3C layer sandwiched between them (Fig. 2-d2), which indicates that the outer Ni_3C shell of the cluster forms after the aggregation of the constituent NPs, *i.e.*, the dendritic morphology of the cluster is locked in by the rigid Ni_3C shell. The Ni_3C shell is relatively thin, compared to the overall dimensions, so in the HRTEM images (Fig. 2-d5 and d6) and the conjugate FFT pattern (Fig. 2-d4), the Ni core's contribution overwhelms that of the Ni_3C shell, and the *d*-spacing ($\sim$1.57 Å) matches $(10\bar{1}2)_{Ni}$.

Platelets (Fig. 1E). The platelets exhibit a narrow distribution in length, with a mean of 39.5 nm and a standard deviation of 3.2 nm (Fig. S1E†); each platelet has two opposite hexagonal basal planes (Fig. 2-e2). When the platelet is sitting on its basal facet (zone axis = $[0001]_{Ni}$) under TEM, a fix-fold symmetry can be observed at the center of the platelet with the *d*-spacing ($\sim$2.30 Å) matching $(10\bar{1}0)_{Ni}$ (Fig. 2-e5 and e6). The FFT pattern (Fig. 2-e4) confirms the origin of symmetry as the $\{10\bar{1}0\}$ facets of HCP Ni, so each platelet has a single crystalline HCP Ni core with $\{10\bar{1}0\}_{Ni}$ as side facets and $\{0001\}_{Ni}$ as basal facets. In addition, the FFT pattern (Fig. 2-e4) does not reveal bright spots other than the ones associated with $\{10\bar{1}0\}_{Ni}/\{11\bar{2}0\}_{Ni_3C}$, and the TEM images show that the platelet has a thin shell of $\sim$50% contrast (Fig. 2-e2 and e3), similar to the case of core@shell dots (Fig. 1C and S3a†). Hence the platelets are also of HCP Ni core@rhombohedral Ni_3C shell structure.

Dendrites (Fig. 1U). The dendrites (Fig. 1U) are derived from the platelets (Fig. 1E). Each dendrite has a proximal hexagonal platelet, of single crystalline HCP Ni with $\{10\bar{1}0\}_{Ni}$ as side facets and $\{0001\}_{Ni}$ as basal facets, and six branches in the platelet's $\langle 11\bar{2}0\rangle_{Ni}$ directions (Fig. 2-f7). Some dendrites are not perfectly symmetrical, but all of the platelets grow with a 6-fold symmetry (Fig. S1U†). Each branch, of similar HCP Ni core@rhombohedral Ni_3C shell structure, is highly crystalline (Fig. 2-f3 and f4) with *d*-spacing ($\sim$1.57 Å) matching $(10\bar{1}2)_{Ni}$ and $(11\bar{2}6)_{Ni_3C}$ (Fig. 2-f5 and f6). Therefore the dendrites comprise a branched HCP Ni core and a thin Ni_3C shell.

Polyhedra (Fig. 1F and G) and their aggregates (Fig. 1J and K). Four morphologies are included in this category: polyhedra (Fig. 1F), polyhedral assemblies (Fig. 1J), polyhedra with stubs on vertices (Fig. 1G), and their assemblies (Fig. 1K).

Polyhedra (Fig. 1F) have well defined facets (Fig. 2-g2); the HRTEM image (Fig. 2-g5 and g6) of a selected surface area (Fig. 2-g3) shows a clear difference in contrast between the Ni core and Ni_3C shell. In addition, the FFT pattern of the surface (Fig. 2-g4) shows a single pair of spots (*d*-spacing ~ 1.57 Å), matching $(10\bar{1}2)_{Ni}$ and $(11\bar{2}6)_{Ni_3C}$. As for the polyhedra with stubs on their vertices (Fig. 1G), with other features being the same as the regular polyhedra (Fig. 1F), they can develop highly-crystalline stubs (Fig. 2-i2) enclosed by $\{0006\}_{Ni_3C}$ and $\{11\bar{2}3\}_{Ni_3C}$ (i5, i6); the FFT pattern (Fig. 2-i4) confirms their single crystallinity.

Polyhedra, with stubs or not (Fig. 1G and F, respectively), can assemble into their corresponding quasi-spherical aggregates (Fig. 1K and J, respectively). Both kinds of aggregates have uneven surfaces (Fig. 2-h2 and j2), because of the intrinsic geometry of the constituent polyhedra. HRTEM images of the selected surface region of both polyhedral aggregates reveal the existence of amorphous surface carbon (Fig. 2-h3, h5, h6, j3, j5 and j6). Therefore we proposed that to form the observed polyhedral aggregates (Fig. 1J and K), the polyhedra (Fig. 1F and G) form HCP Ni core@Ni_3C shell structures, assemble according to their intrinsic geometry, and eventually accumulate some amorphous carbon on the surface by catalyzing the decomposition of hydrocarbon ligands.

Urchins (Fig. 1V). As revealed by the SEM image of a Focused Ion Beam (FIB)-milled cross-section (Fig. S4†), each urchin (Fig. 1V) has a central spherical core with serrated rim, suggesting that the core resembles the aggregates of polyhedra without stubs in Fig. 1J. The branches on an urchin are highly crystalline, as shown by the clear $(10\bar{1}2)_{Ni}$ fringes (Fig. 3-k2 and k3); and they grow along $[0001]_{Ni}$, as indicated by the parallel $(0002)_{Ni}$ fringes (Fig. 3-l5 and l6). Similar to many aforementioned nanostructures, the shape of an urchin, which is largely determined by the shape of the Ni core, is also locked in by a Ni_3C shell, shown clearly by the HRTEM images of a branch in Fig. 3-l2 and l3. A further look at the surface of a branch (Fig. 3-k5 and k6) reveals that the *d*-spacing matches $(10\bar{1}2)_{Ni}$ near the axis and $(11\bar{2}6)_{Ni_3C}$ near the surface. Despite the highly hierarchical structure, urchins can be synthesized with high uniformity (Fig. S1N, R and V†).

Dandelions with short (Fig. 1W), long (Fig. 1X), or melted (Fig. 1H) branches. Dandelions can also be synthesized with high uniformity (Fig. S1†). Similar to the case of urchins, a dandelion also has a central spherical core that is probably the result of the aggregation of polyhedra, as revealed by the SEM image (Fig. S5†) of FIB-milled cross-section of a typical dandelion with short branches (Fig. 1W). The branches on the dandelions grow in the direction of $[0001]_{Ni}$, similar to the ones on an urchin, but on the end of each branch on a dandelion, there is a platelet of hexagonal symmetry, as shown by the HRTEM images and FFT pattern acquired from the $[0001]_{Ni}$ direction (Fig. 3-p2–p6). A typical platelet on the branch of the dandelions, regardless of the branch being short (Fig. 1W) or long (Fig. 1X), is of an HCP Ni core enclosed by $\{10\bar{1}0\}_{Ni}$ side facets, and $\{0001\}_{Ni}$ basal facets, and a Ni_3C shell enclosed by $\{0006\}_{Ni_3C}$ and $\{11\bar{2}3\}_{Ni_3C}$, as proven by the side-view HRTEM images and FFT pattern of the platelet (Fig. 3-o2–o6). Moreover, in the TEM images of the top facet of a platelet (Fig. 3-m2 and m3), the difference in contrast clearly indicates the boundary between Ni and Ni_3C; when the boundary is imaged closely (Fig. 3-m5 and m6), the minute difference between $(0002)_{Ni}$ and $(0006)_{Ni_3C}$ can be revealed, so the platelet is also of the HCP Ni core@Ni_3C shell structure. The Ni core of the platelet is largely of HCP phase, because at the reaction temperature (~280 °C), the HCP Ni phase is more stable than the Face-Centered Cubic (FCC) phase and thus dominates in the Ni core, as shown by the HRTEM images (Fig. 3-n2 and n3), and the XRD patterns (Fig. S2j, k and l†).[23] However, stacking faults may be present and can lead to occasional FCC zones, as revealed by the HRTEM images in Fig. 3-n5 and n6 and illustrated in the mechanistic scheme in Fig. 5-e1.

Besides the aforementioned platelets on the pristine dandelions (*e.g.*, Fig. 1W or X), after extended heating (120 min), a platelet and its vicinal branch segment in a pristine dandelion can reconstruct into a bulb (Fig. 3-r1), leading to a dandelion species of a melted morphology (Fig. 1H). For the melted platelet, its top $(0002)_{Ni}$ facets are well preserved and remain flat (Fig. 3-r2 and r3), but its side facets (Fig. 3-r5 and r6) and junctions (Fig. 3-q2–q6) undergo significant reconstruction, compared with the pristine platelet on a branch (Fig. 3-o2 and o3).

Parametric analysis

Parametric analysis links the NBC morphologies in Fig. 1 to synthesis parameters, *i.e.*, reaction temperature, heating duration, heating rate, and the identity and concentration of the precursors, ligands, and solvent. To rationally probe this vast parameter space, reaction temperature, solvent identity, and precursor were fixed as constants to reduce the complexity of the parameter space while maintaining the access to adequately diverse morphologies.[24] Then univariate experiments were performed by varying each selected synthesis parameter to observe the induced morphological shift. Every univariate experiment is noted by an arrow linking two panels in Fig. 1: single arrows indicate the morphological shift induced by the increase of a parameter, *e.g.*, arrow <1, B→A, PL> (PL for promoting ligand) signifies that the morphology shifts from dots (Fig. 1B) to clusters (Fig. 1A) with an increase of the concentration of dodecylamine (DDA) as a promoting ligand; double arrows indicate the morphological shift induced by the switch of a parameter, *e.g.*, arrow <2, B↔D, LS> (LS for ligand species) indicates that the morphology shifts between dots (Fig. 1B) and shells (Fig. 1D) as the ligands species toggles between oleic acid (OA) and trioctylphosphine (TOP).

Heating rate. Two heating rates (HRs) were used to reach the reaction temperature (280 °C). Because the high-temperature solution phase synthesis of nanostructures is highly sensitive to the heating rate,[25] the increase of HR from ~3.42 °C min^{-1} to

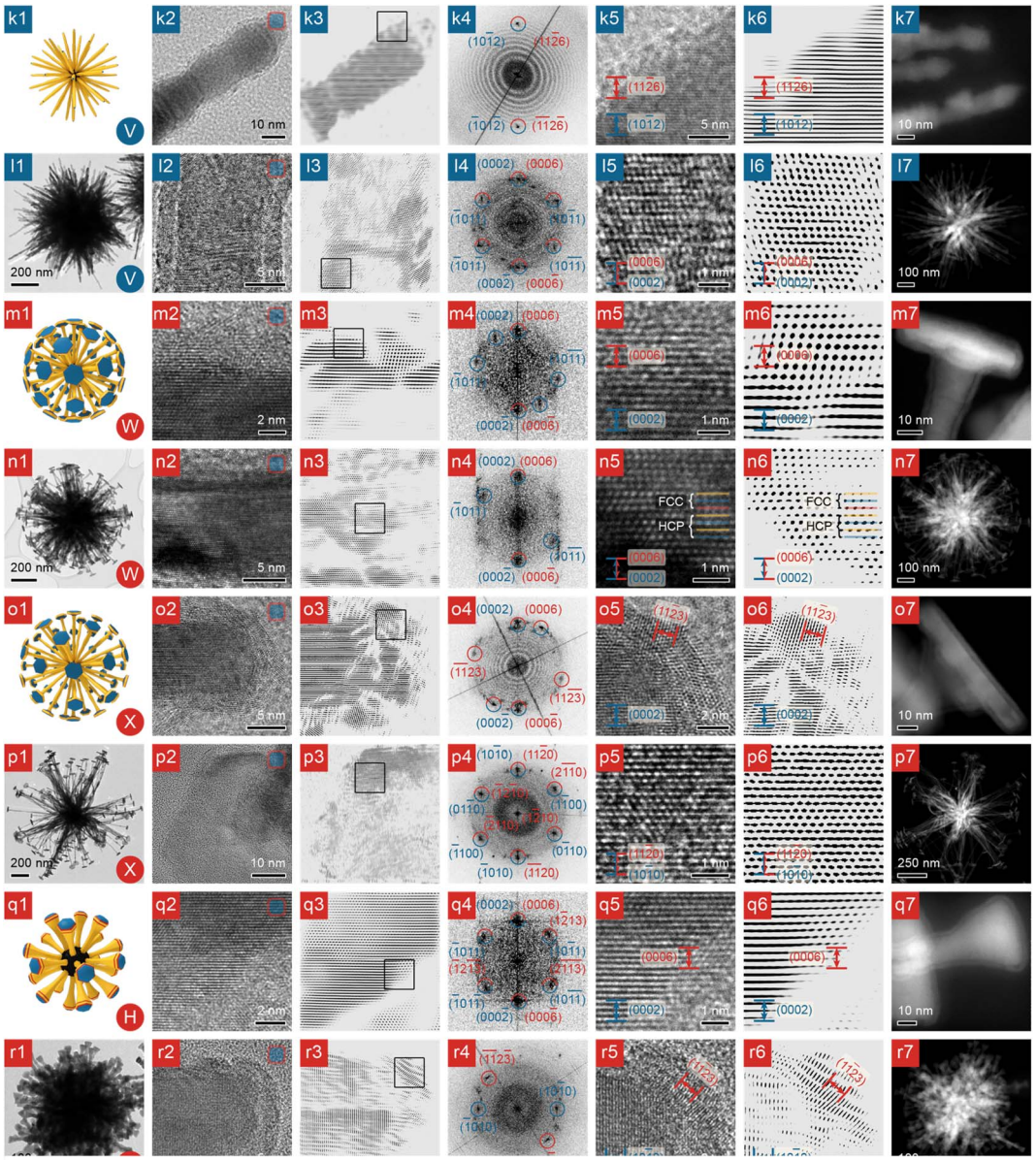

Fig. 3 Structural and compositional analyses of NBCs, part 2. (k and l) Urchins; (m and n) dandelions; (o and p) larger dandelions; (q and r) dandelions with bulbs. Column 1: 3D model (the inset at the lower right corner is the morphology's serial number from Fig. 1); column 2: TEM image (the inset at the upper right corner represents the chemical composition of the NBC: blue represents Ni; orange Ni_2P; red Ni_3C); column 3: FFT-filtered TEM image (the square indicates the region enlarged in column 5); column 4: indexed FFT pattern of the HRTEM image in column 5 (spots of Ni labelled in blue; Ni_3C in red); column 5: HRTEM image (facets of Ni indexed in blue: Ni_3C in red); column 6: FFT-filtered HRTEM image; column 7: HAADF STEM image. Scale bars are shared by column 2 and 3, and by column 5 and 6.

$\sim$5.26 °C min^{-1} is significant enough to dramatically change the morphology. As the HR increased, for <6, G→F, HR>, the surface stubs on the polyhedra disappeared; for <17, O→N, HR>, the dandelions transitioned to the urchins. Therefore, we conclude that the slow HR ($\sim$3.42 °C min^{-1}) allowed the formation of 2D substructures, *i.e.*, the stubs on the polyhedra (Fig. 1G and K) and the platelets on the dandelion branches (Fig. 1O and W).

Time. As elaborated above, most NBCs in this report were locked in by a thin layer of surface carbide and can steadily maintain their morphologies, but in order to evaluate the most complex morphology's structural robustness, the dandelions were aged for an additional 30 min (indicated by <13, L→H, TM> (TM for time)). In this case, although the platelet on each branch reconstructed into a bulb with reduced surface area and smoothed curvature, the branched "dandelion" morphology maintained its hierarchy.

Solvent. 1-Octadecene (ODE) was chosen as the non-coordinating solvent;[3] adjusting the solvent volume (SV) proved efficient for tuning the size of the dendrites from 309 nm (Fig. 1I) to 494 nm (Fig. 1M) (<7, I→M, SV>); urchins from 390 nm (Fig. 1N) to 527 nm (Fig. 1R) (<16, N→R, SV>); and

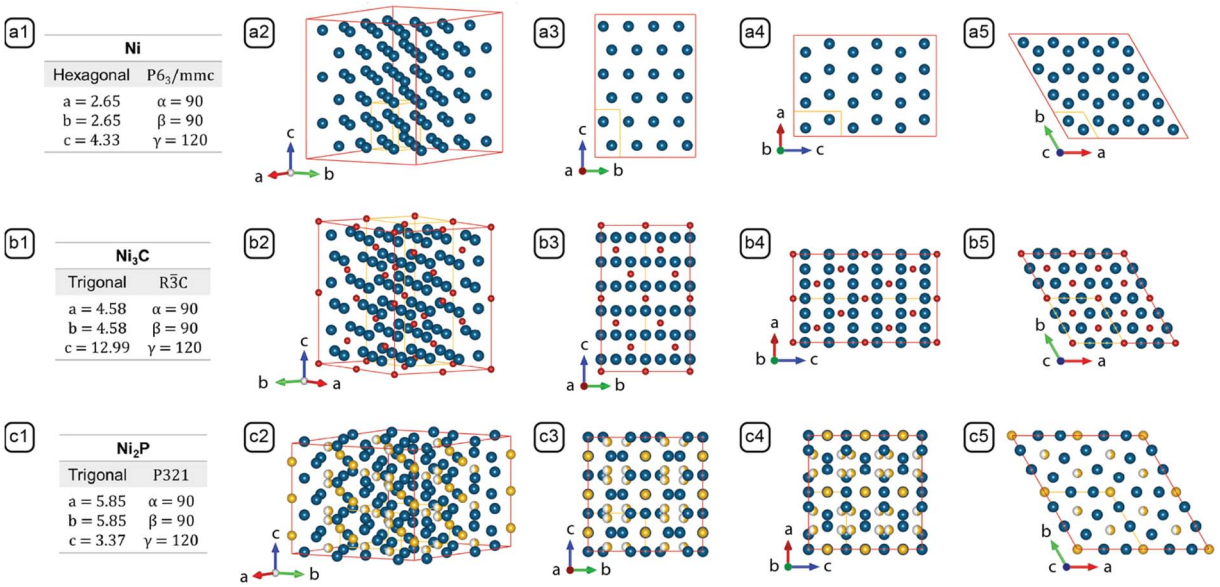

Fig. 4 Lattice parameters and crystal structures of (a) Ni (PDF #45-1027), (b) Ni_3C (PDF #06-0697), and (c) Ni_2P (PDF #65-9706). Columns: (1) Stoichiometry, crystal system, space group and lattice parameters; (2) crystal model projected along the standard orientation;[31] (3) crystal model projected along [10$\bar{1}$0]; (4) crystal model projected along [01$\bar{1}$0]; (5) crystal model projected along [0001]. The models outlined by the red edges in columns 2, 3, 4, and 5 consist of multiple unit cells to reveal the resemblance between Ni and Ni_3C, and the difference between Ni_2P and the former two. The unit cell of each crystal is represented by the yellow lines.

dandelions from 426 nm (Fig. 1O) to 505 nm (Fig. 1S†) (<18, O→S, SV>).

Ligands. Ligands that modulate the NBC morphologies can be sorted into three categories by function: promoting ligands (PL), etching ligands (EL), and neutral ligands.

Promoting ligands include dodecylamine (DDA) and oleylamine (OAm), both of which are Brønsted bases that reduce the precursor ($Ni(acac)_2$) to monomer (Ni^0) *via* a two-electron route to increase the monomer concentration [*m*].[26] In this study, concentration of the promoting ligand affected the morphology remarkably. Increasing the amount of OAm from 3 mmol to 7.6 mmol raised the monomer's formation rate and concentration, and hence led to the enlargement of the dendrite's size from 525 nm to 579 nm (<19, Q→U, PL>). However, increasing the [DDA] from zero to low or high concentration exhibited diverse effects. Starting from the absence of DDA, adding 20 mmol of it to a recipe promoted the NBC's 2D growth, *i.e.*, the platelets developed into dendrites (<5, E↔I, LS>). Starting from a low [DDA], more DDA increased the [*m*] to form more dots, which then clustered, because ligand passivation was still inadequate at this point (<1, B→A, PL>). Starting with a relatively high [DDA], the properly passivated dots grew into individual polyhedra, which then assembled into polyhedral aggregates (<3, B→J, PL>); alternatively, starting with even higher [DDA], the polyhedra were better passivated and protected, and thus remained freestanding (<8, J→F, PL>, <10, K→G, PL>).

Etching ligand refers to OA that could etch down the Ni.[27,28] As a Brønsted acid, OA can form an acid–base complex with OAm to suppress the monomer formation, so as the [OA] increased, [*m*] decreased, leading to the formation of smaller NBCs (<4, C→B, EL>). For the branched NBCs, the increased amount of OA led to similar nanostructures with less branches (<21, S→L, EL>).

Neutral ligands, not impacting the [*m*] or etching down the NBCs, include TOP and 1,2-tetradecanediol (TDD). Switching from OA to TOP transformed Ni dots to Ni_2P shells *via* the incorporation of phosphorus (<2, B↔D, LS>);[29,30] switching from DDA to TDD induced the branching of polyhedral aggregates into dandelions (<12, K↔O, LS>).

Growth models

After characterizing the NBCs' morphologies and analyzing the synthesis parameters, the formation mechanism of the NBCs can be rationalized in two steps: first, we define the models for each growth stage based upon basic thermodynamic and kinetic principles; second, we use those models as building blocks to establish a holistic framework of the formation mechanisms (Fig. 5).

Growth models can usually be constructed based upon the dominant facets' chemical potentials and the monomer's deposition barriers as the key thermodynamic and kinetic factors, respectively. To assist the understanding of growth mechanism, the relevant crystal structures have been illustrated in Fig. 4. HCP Ni was adopted as the model system for elaborating the growth mechanism for the following reasons. Firstly, the Ni core formed before the Ni_3C shell, so the branching mechanism originated from Ni. Secondly, the carburization of HCP Ni to Ni_3C is isomorphic, which is demonstrated by the similarity between HCP Ni and Ni_3C (Fig. 4), *i.e.*, during the carburization process, the positions of the Ni atoms in HCP Ni only changed slightly (Fig. 5-b5). Thirdly, the equilibrated Ni_3C

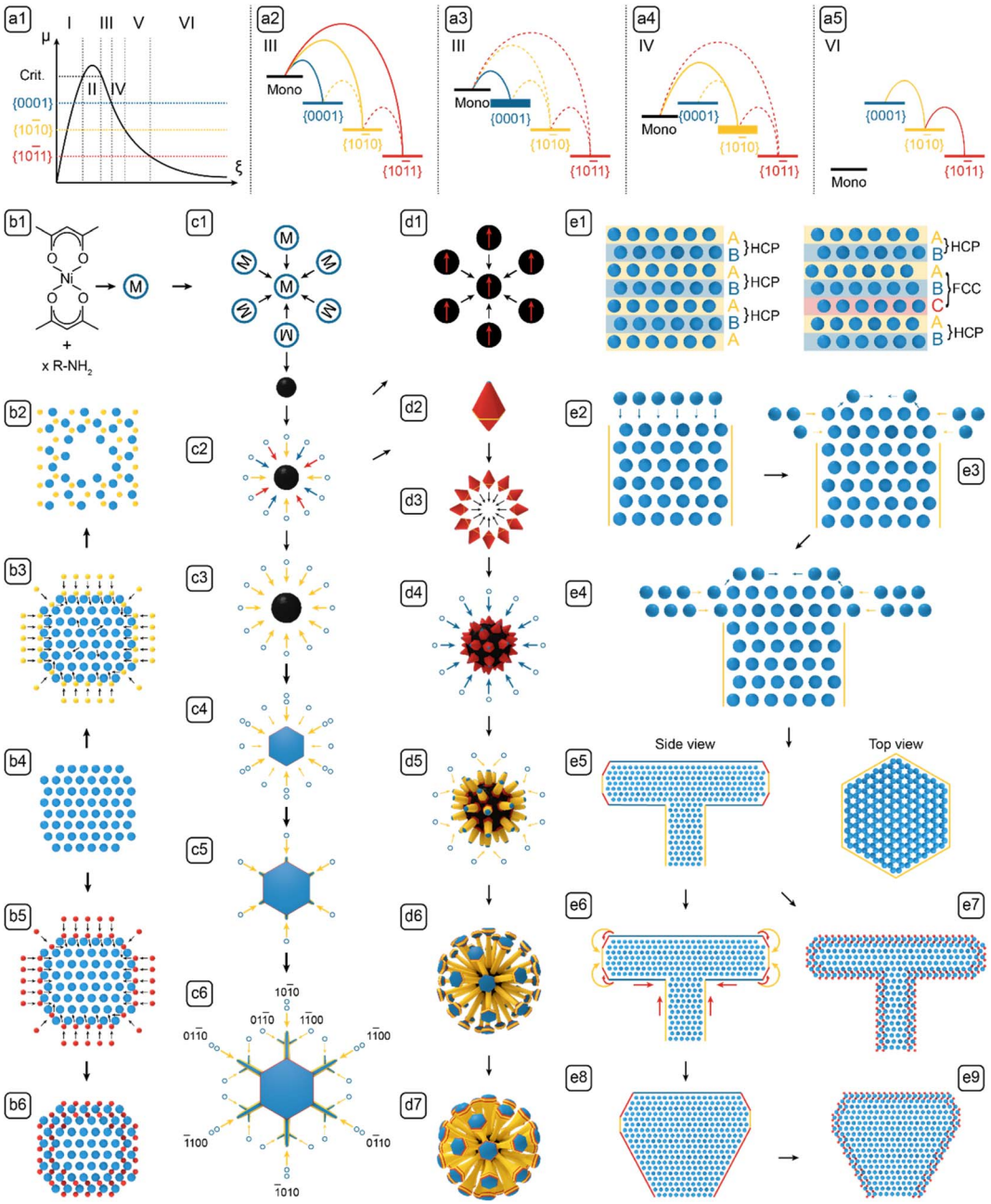

Fig. 5 The formation mechanisms of NBCs. (a1) The LaMer diagram; chemical potential diagrams for (a2) nascent growth, (a3) 1D growth, (a4) 2D growth, and (a5) 3D reconstruction. (b1) Transformation of precursor to monomer. (c1) Nucleation. (c2) Nascent growth. (c3) 2D growth. (c4) Protrusion of tips. (c5) Branching. (c6) Sub-branch formation. (d1) Aggregation of dots into clusters. (d2) Polyhedron. (d3) Aggregation of polyhedra. (d4) 1D growth of surface protrusions. (d5) 2D growth on branches. (d6) Dandelion. (d7) Dandelion with bulb. (b2) Ni_2P shell. (b3) Phosphorization. (b4) Ni dot. (b5) Carburization. (b6) Core@shell dot. (e1) HCP *vs.* HCP + FCC. (e2) 1D growth. (e3) Edge-sharpening instability. (e4) 2D growth. (e5) Side and top views of platelet-on-branch structure. (e6) 3D reconstruction. (e7) Carburized platelet-on-branch structure. (e8) Bulb structure. (e9) Carburized bulb structure. The blue, yellow, and red arrows represent the growth on $\{0001\}_{Ni}$, $\{10\bar{1}0\}_{Ni}$, and $\{10\bar{1}1\}_{Ni}$ facets, respectively. Note that the latter proximal morphology results from the former process, *e.g.*, the platelet in c4 results from the selective growth of $\{10\bar{1}0\}_{Ni}$ in c3.

shell of an NBC is conformal to the Ni core (Fig. S3†). As a result, the morphological evolution of the HCP Ni core can be inspected to derive the branching mechanism of the corresponding NBC nanostructure.[18]

Because the NBCs comply with the Bravais rule, the exposed Ni facets are the low-index planes of greatest lattice-point densities, *i.e.*, $\{10\bar{1}0\}_{Ni}$, $\{0001\}_{Ni}$ and $\{10\bar{1}1\}_{Ni}$, the chemical potentials of and the deposition barriers on which can be analyzed and ranked. First, the "platelet-on-branch" structures reconstructed into bulbs (Fig. 5-e6). $\{0001\}_{Ni}$ and $\{10\bar{1}0\}_{Ni}$ rearranged into $\{10\bar{1}1\}_{Ni}$, indicating that $\mu_{\{10\bar{1}1\}_{Ni}}$ has the lowest chemical potential. Second, $\{10\bar{1}1\}_{Ni}$ lacked noticeable growth.

Even when the monomer chemical potential (μ_m) was higher than any participating facet, $\{10\bar{1}1\}_{Ni}$ never grew noticeably compared with $\{0001\}_{Ni}$ and $\{10\bar{1}0\}_{Ni}$, indicating that the highest deposition barrier is on $\{10\bar{1}1\}_{Ni}$, *i.e.*, $\Delta E_{m,\{10\bar{1}1\}_{Ni}}$. Third, compared with $\{10\bar{1}0\}_{Ni}$, $\{0001\}_{Ni}$ has lower lattice-point density, lower ligand density, higher chemical potential, and lower deposition barrier. Thus the chemical potentials can be ranked as $\mu_{\{0001\}_{Ni}} > \mu_{\{10\bar{1}0\}_{Ni}} > \mu_{\{10\bar{1}1\}_{Ni}}$; the deposition barriers as $\Delta E_{m,\{10\bar{1}1\}_{Ni}} > \Delta E_{m,\{10\bar{1}0\}_{Ni}} > \Delta E_{m,\{0001\}_{Ni}}$.

With the ranked chemical potentials and deposition barriers, we can establish the qualitative diagrams (Fig. 5-a1–a5) to rationalize the formation mechanisms of all NBCs (Fig. 5-b1–e9). After nucleation, the subsequent growth could follow various paths to form the different morphologies in Fig. 1. However, for the classical diffusional growth of most NBCs, only five steps, *i.e.*, nucleation, nascent growth, 1D growth, 2D growth, and 3D reconstruction, occur as the monomer concentration [m] decreases in time.[19] Besides the diffusional growth, non-classical models, *i.e.*, aggregation and carburization, are also introduced to complete the palette of models for deconvoluting the formation mechanisms of all the NBCs.

Nucleation. Precursors transform to monomers (Fig. 5-b1), which then continuously accumulate before nucleation.[26] In the classic LaMer model (Fig. 5-a1),[19] when [m] exceeds the critical supersaturation, nucleation occurs spontaneously (Fig. 5-c1), and then ceases as the supersaturation is partially relieved. Because the nucleation rate and duration depend on the kinetics of monomer generation/consumption, they are readily tunable, especially by the heating rate and the solvent volume. On one hand, with a slower heating rate, the nucleation extends in duration,[32] consumes more monomers, generates more nuclei, and leaves a lower [m] (and accordingly a lower μ_m) for subsequent growth. On the other hand, with a larger ODE volume, the [m] decreases; nucleation consumes less monomers to form fewer nuclei; more monomers remain available for further growth; eventually, larger NBCs can form.

Nascent growth. The principles for the growth of any facet should be elucidated first. Thermodynamically driven by the difference between the monomer's chemical potential (μ_m) and the target facet's chemical potential ($\mu_{\text{target facet}}$), the monomers diffuse towards, attach to, and integrate into the target facets. Note that the μ_m is a function of the monomer activity, *i.e.*, the product of γ_m and χ_m (eqn (1)). When χ_m is low, γ_m can approach its infinite dilution value ($\gamma_m{}^{\infty}$), so μ_m can be assumed to only depend upon χ_m. Kinetically, according to eqn (2), the monomers must deposit at a reasonably high rate ($r_{m,\{hkil\}}$), which necessitates a high [m] and/or a low deposition barrier ($\Delta E_{m,\{hkl\}}$) at the target facet. $\Delta E_{m,\{hkil\}}$ can be lowered by decreasing the ligand concentration to reduce the surface ligand density or switching to a relatively weakly bound ligand.

$$\mu_m = \mu_m^{\ominus} + RT \ln \gamma_m \chi_m \quad (1)$$

Eqn (1): the activity of monomer. μ_m is the monomer chemical potential; $\mu_m^{\ominus}$ the standard monomer chemical potential; γ_m the activity coefficient of monomer; χ_m the mole fraction of monomer.

$$r_{m,\{hkil\}} = k_{m,\{hkil\}}[m]^a = A e^{-\frac{\Delta E_{m,\{hkil\}}}{RT}}[m]^a \quad (2)$$

Eqn (2): the deposition rate of monomers on {*hkil*} facets. $k_{m,\{hkil\}}$ is the rate constant; A the pre-exponential factor; $\Delta E_{m,\{hkil\}}$ the deposition barrier of monomer on {*hkil*}; [m] the monomer's molar concentration; and a the reaction order.

Now we can define the nascent growth as the 3D isotropic growth of multiple facets that happens immediately after nucleation (Fig. 5-c2). Because the chemical potentials rank as $\mu_m \gg \mu_{\{0001\}_{Ni}} > \mu_{\{10\bar{1}0\}_{Ni}} > \mu_{\{10\bar{1}1\}_{Ni}}$ (Fig. 5-a2), the monomers are thermodynamically allowed to deposit on $\{0001\}_{Ni}$, $\{10\bar{1}0\}_{Ni}$, and $\{10\bar{1}1\}_{Ni}$. If the nascent growth was transient, the nuclei would grow into primary dots; if the nascent growth persisted, the dots would further grow into polyhedra.[1] The collective growth of all facets also indicates an ample supply of monomers *via* diffusion, so the nascent growth is reaction-controlled.[33]

Anisotropic growth. Anisotropic growth includes both 1D growth and 2D growth. Following the isotropic nascent growth, either 1D or 2D growth mode places more kinetic requirements on the monomer deposition and the surface diffusion. That being said, on different facets, the monomer deposition barriers and deposition rates must vary to follow the anisotropic attachment kinetics. In addition, the edge diffusion must have a high Ehrlich–Schwoebel barrier to retain the deposited atoms on the target facets, so the edge diffusion, *e.g.*, from $\{0001\}_{Ni}$ to $\{10\bar{1}0\}_{Ni}$, is sufficiently slow to preserve the anisotropic, branched morphology that formed during the anisotropic growth.

1D growth. 1D growth preferentially occurs on $\{0001\}_{Ni}$, and produces nanorods with $\{10\bar{1}0\}_{Ni}$ as side facets and $\{0001\}_{Ni}$ as basal facets (see the illustration for the morphological shift of the NBCs in Fig. 5-d4 and d5, and the corresponding atomic models in Fig. 5-e2). In this mode, the chemical potentials rank as $\mu_m > \mu_{\{0001\}_{Ni}} > \mu_{\{10\bar{1}0\}_{Ni}} > \mu_{\{10\bar{1}1\}_{Ni}}$ (Fig. 5-a3), so all of the $\{10\bar{1}0\}_{Ni}$, $\{0001\}_{Ni}$ and $\{10\bar{1}1\}_{Ni}$ facets are thermodynamically allowed to grow. As the monomers are being consumed, the driving force for their diffusion to the surface weakens gradually. When the supply of monomers becomes inadequate,[34] the three groups of facets start competing for monomers, and hence the rate determining step (RDS) shifts from reaction to diffusion. At this point, $\{0001\}_{Ni}$ has the lowest deposition barrier, so it grows at the fastest rate according to eqn (2). Moreover, due to the Berg effect,[1] the protrusions on the polyhedral aggregates (Fig. 1J and K) experience a higher [m], so their $(0002)_{Ni}$ facets consume most of the monomers to grow into the 1D branches on urchins or dandelions. The developed 1D branch cannot be of perfect internal or external structure. First, in each branch, the Ni atoms stack along the $[0001]_{Ni}$ direction following the "A-B-A" HCP pattern,[35] but occasionally stacking faults may be introduced by thermal fluctuation to form "A-B-C-A" FCC zones (see the atomic models in Fig. 5-e1).[36] Second, as the [m] fluctuates with temperature and geometry in the vicinal area of developing branches, the growth may shift between the reaction-controlled nascent growth and the diffusion-controlled 1D growth, so the relative deposition rates

on $\{0001\}_{Ni}$ and $\{10\bar{1}0\}_{Ni}$ of the developing branches oscillate to cause a variation of the branch diameter along the axial direction (Fig. 3-k2).

2D growth. Both nascent growth and 1D growth can be followed by 2D growth. In this mode, the regio-selective deposition on $\{10\bar{1}0\}_{Ni}$ is accentuated to form 2D structures with $\{10\bar{1}0\}_{Ni}$ as side facets and $\{0001\}_{Ni}$ as basal facets, including the freestanding platelets or dendrites (see the illustrations in Fig. 5-c3→c6) and the platelets on dandelion branches (see the illustrations in Fig. 5-d5→d6). During the 2D growth, the chemical potentials rank as $\mu_{\{0001\}_{Ni}} > \mu_m > \mu_{\{10\bar{1}0\}_{Ni}} > \mu_{\{10\bar{1}1\}_{Ni}}$ (Fig. 5-a4), so the growth of $\{0001\}_{Ni}$ is thermodynamically prohibited. In addition, to form the 2D nanostructures, a general principle is that the specific edge energy and the specific surface energy should be high and low, respectively.[37,38] When this requirement was met, the deposition of monomers on the wide facets (*i.e.*, $\{10\bar{1}0\}_{Ni}$ side facets of branches, or $\{0001\}_{Ni}$ basal facets of platelets) would introduce energetically expensive edges, but the deposition on the narrow facets (*i.e.*, $\{0001\}_{Ni}$ basal facets of branches, or $\{10\bar{1}0\}_{Ni}$ side facets of platelets) would cover those facets to create only inexpensive surfaces, so the deposition on the narrow facets is preferred. Therefore to encourage the 2D growth, surface passivation with strong ligands is necessary to lower the specific surface energy.[37]

As for the growth kinetics, 2D platelets and 2D dendrites both have diffusion of monomers to the surface as RDS,[39] but the two nanostructures differ in attachment kinetics as follows.

For the 2D platelets, both of $\{10\bar{1}0\}_{Ni}$ and $\{10\bar{1}1\}_{Ni}$ are thermodynamically allowed to grow, but the growth of $\{10\bar{1}1\}_{Ni}$ is kinetically hindered by its high deposition barrier, so only the $\{10\bar{1}0\}_{Ni}$ grows significantly. In this case, the 0D dots can develop into the freestanding 2D platelets (see Fig. 5-c3→c4), and the tips of the 1D branches can develop into the 2D platelets on branches (see Fig. 5-d5→d6). The symmetry breaking that occurred during the transition of 0D dots or 1D rods into 2D platelets is a crucial concept that deserves further elaboration. At the $\{0001\}_{Ni}$ basal facets of the 0D dots or 1D branches, the edges and vertices are sharpened by the Berg effect by promoting the growths thereof, but simultaneously they are blunted by the Gibbs–Thomson effect (eqn (3)) that encourages the movement of surface atoms from the edges and vertices of high curvature to the flat facets of lower curvature (see the illustration in Fig. 5-e3), so as a result, the involved $\{0001\}_{Ni}$ basal facets are slightly concave in the center and rounded around the edges and vertices. In addition, because the growth of $\{0001\}_{Ni}$ is prohibited, the growth following the $\langle 10\bar{1}0\rangle_{Ni}$ direction narrows out the outermost $\{10\bar{1}0\}_{Ni}$ terrace. In return, the deposition barrier on $\{10\bar{1}0\}_{Ni}$ is further lowered to promote its growth (Fig. 5-e4).[37] This self-reinforcing phenomenon, named Edge Sharpening Instability (ESI), drives the platelet formation *via* a loop of positive feedbacks.[1] Moreover, the relative positions of $\mu_{\{10\bar{1}0\}_{Ni}}$ and $\mu_{\{0001\}_{Ni}}$ (*i.e.*, $\mu_{\{10\bar{1}0\}_{Ni}} < \mu_{\{0001\}_{Ni}}$) creates a high barrier that hinders the edge diffusion from the $\{10\bar{1}0\}_{Ni}$ side facets to the $\{0001\}_{Ni}$ basal facets, so the platelet-on-branch structure can be retained effectively (see the illustration of the structure in Fig. 5-e5).[40]

For the 2D dendrites, the 2D platelets sprout from the six corners to form those, following a crystal habit similar to that of the snowflakes. Abiding by the Wilson-Frenkel rule,[41] a platelet's side facets grow in proportion to the level of monomer supersaturation. However, three factors synergistically encourage the protrusion of the 2D platelets' corners and vertices (see the illustration of a 2D platelet with protruding corners in Fig. 5-c5). First, the atoms at the corners and vertices have lower coordination numbers and thus possess higher energies; second, their high surface curvatures reduce the local ligand density and hence lowers the deposition barrier thereof; third, their driving force of growth is enhanced by the Berg effect.[1] Therefore, with high surface energy, low deposition barrier, and high driving force, the corners and vertices protrude under the effect of the Mullins-Sekerka Instability (MSI).[1] In turn, the protruded parts experience even higher surface energy, lower deposition barrier, and higher driving force, so eventually, they grow into branches, by a self-reinforcing runaway process similar to the ESI effect. In addition, the dendrite branches are subject to fluctuating μ_m, and occasionally can develop sub-branches (see the morphological shift from Fig. 5-c5 to c6).

3D reconstruction. The platelet-on-branch structure on the dandelion is highly robust, but under the persistent heating at 280 °C, it can still be gradually transformed to a bulb structure *via* the 3D reconstruction (Fig. 5-e5→e6→e8) and then be locked in by surface carburization (Fig. 5-e8→e9). Thermodynamically, the chemical potentials rank as $\mu_{\{0001\}_{Ni}} > \mu_{\{10\bar{1}0\}_{Ni}} > \mu_{\{10\bar{1}1\}_{Ni}} > \mu_m$ (Fig. 5-a5), so the direct growth of all facets is prohibited, and thus only the diffusion of surface atoms from $\{0001\}_{Ni}$ to $\{10\bar{1}0\}_{Ni}$ and $\{10\bar{1}1\}_{Ni}$ is still in effect (see the directions of diffusion noted with the arcs in Fig. 5-e6). The edge diffusion between the adjacent facets is effectively stimulated by the energy provided by the prolonged heating at 280 °C (noted by the curved arrows in Fig. 5-e6). Moreover, under the Gibbs–Thomson effect (eqn (3)), the chemical potentials can vary according to the surface curvatures of the convex, flat, and concave areas, *i.e.*, $\mu_{convex} > \mu_{flat} > \mu_{concave}$, so the nanostructure's surface undergoes a process that blunts out the convex corners and vertices to fill the concave junctions (noted by the straight arrows in Fig. 5-e6).[42] These two pathways, *i.e.*, the diffusion between different groups of facets and the diffusion between the convex and concave parts, synergistically reshape the platelet-on-branch structure (Fig. 5-e5) to a bulb structure with reduced surface area and surface energy (Fig. 5-e8).

$$\mu_r = \mu_b + \frac{2\sigma V_m}{rRT} \tag{3}$$

Eqn (3): Gibbs–Thomson equation. μ_r is the chemical potential of surface with radius of curvature r; μ_b the chemical potential of flat surface; σ the specific surface energy; V_m the molar volume; r the radius.

Kinetically, this reconstruction process only becomes significant upon extended heating, so it is apparently slow enough to retain the platelet-on-branch structure.[1] This observation directly proves that the branched NBCs are kinetically trapped in non-equilibrium shapes, and their morphological

evolution follows the Ostwald–Lussac Law,[43,44] *i.e.*, a thermodynamically unstable system can transform to stabilize *via* a series of intermediate states.

Additional models. Besides the various models of diffusional growth, additional models including aggregation and carburization are introduced to complete the framework of NBCs' formation mechanisms.

Aggregation. To minimize the surface energy, smaller NPs can aggregate *via* various pathways. The dots (Fig. 1B) can aggregate into single crystalline clusters (Fig. 1A) *via* the oriented attachment mechanism (see the schematic illustration in Fig. 5-d1); the quasi-bipyramidal polyhedra (Fig. 1F or G) can pack into the spiky cores of urchins (Fig. 1J) or dandelions (Fig. 1K) (see the schematic illustration in Fig. 5-d3).

Carburization. The surface carburization can lock in the complex morphologies (Fig. 5-e7 and e9) and thus enable a convenient exploration of the NBCs' morphologies. To better understand its mechanism, here we compare it side-by-side with an analogous process, *i.e.*, phosphorization. The Ni dots can catalyze the decomposition of hydrocarbon chains, to accumulate some carbonaceous species on the surface and initiate the carburization process.[18] Therefore, the chemical potential of the carbonaceous species μ_C is higher on the surface, so the carbon atoms diffuse inwards (see the schematic illustration of the carbon atoms' diffusion in Fig. 5-b5). For Ni, the chemical potential of the nickel species μ_{Ni} is higher in the core, so the nickel atoms tend to diffuse outwards, but the carbon atoms diffuse inwards at a much faster rate to form the rigid conformal Ni_3C shell to prevent any noticeable migration of the nickel atoms. As a result, the positions of the Ni atoms in the Ni_3C phase are similar to those in the HCP Ni phase, as illustrated by their crystal models (Fig. 4a and b). In the case of phosphorization (see the schematic illustration in Fig. 5-b4 → b3 → b2), the phosphorus atoms diffuse inwards, but this process is not isomorphic, because of the disparate lattice structures of the HCP Ni and the hexagonal Ni_2P (Fig. 4a and c).[29,30] Moreover, governed by the Kirkendall effect, the outward diffusion rate of Ni is comparable to the inward diffusion rate of P, so the Ni dots (Fig. 1B) hollow out to form the Ni_2P shells (Fig. 1D). These two competing phase transformations can be used to tune the composition of the NBC nanostructures.

Formation mechanisms of the NBCs

"Nature is an endless combination and repetition of a very few laws".[45] Echoing this, the formation mechanism of each NBC can be readily constructed with the models defined above.

0D dots. The dots form *via* these steps: monomer accumulation (Fig. 5-b1), nucleation (Fig. 5-c1), and nascent growth (Fig. 5-c2). Moreover, the dots may transform into Ni core@Ni_3C shell *via* carburization (Fig. 5-b5), or form Ni_2P shells *via* phosphorization (Fig. 5-b3). Alternatively, the dots may also aggregate into single crystalline clusters *via* oriented attachment (Fig. 5-d1).

2D platelets and dendrites. By 2D growth, the dots can develop into platelets under the ESI effect (Fig. 5-c4); the platelets may branch into dendrites under the MSI effect (Fig. 5-c5).

3D urchins. When the nascent growth is sustained, the dots can grow into polyhedra (Fig. 5-c2 → d2). Then the polyhedra can aggregate into polyhedral aggregates as the cores for urchins and dandelions (Fig. 5-d3 → d4). Subsequently, the polyhedral aggregates can develop into urchins *via* 1D growth (Fig. 5-d4 → d5).

3D dandelions. The urchins can develop into dandelions *via* 2D growth at the tips of the 1D branches (Fig. 5-d5 → d6). In addition, under persistent heating, the platelet-on-branch nanostructures on dandelions may reconstruct to form bulbs (Fig. 5-d6 → d7).

Tuning the branched morphologies

With the above information on the NBC morphologies, the synthesis parameters, and the formation mechanisms, now we are in a position to analyze and validate certain synthesis parameters' effect on the morphology from a mechanistic perspective. Some of the most useful synthesis techniques have been further tested and verified as follows.

NP size. The NP size can be adjusted by changing the solvent volume. To enlarge a certain NBC, the most efficient route is increasing the solvent volume to lower the supersaturation level of monomers. Then the nucleation would consume a smaller fraction of monomers to generate fewer nuclei, leave more monomers for the subsequent growth in either nascent, 1D, or 2D growth modes, and finally produce larger NBCs while retaining the morphology. To validate this, we increased the solvent volume in a recipe of dendrite synthesis from 18 mL to 20 mL, and as a result, the dendrite size was enlarged from 494 nm to 525 nm (Fig. 1 <15, M → Q, SV>). Similarly, for the synthesis of urchins, increasing the solvent volume from 25 mL to 30 mL enlarged the NP size from 527 nm to 709 nm (Fig. 1 <20, R → V, SV>); for the synthesis of dandelions, increasing the solvent volume from 19.5 mL, to 30 mL, and then to 35 mL enlarged the NP size from 505 nm, to 816 nm, and then to 1096 nm (Fig. 1 <22, S → W, SV>, <26, W → X, SV>).

Branching. The onset of branching can be induced by neutral ligands. The design and synthesis of branched nanostructures hinge on controlled symmetry breaking, and the key to that is a moderate surface ligand coverage. This ideal coverage must be high enough to provide adequate steric hindrance to constrain the individual dots to grow into polyhedra (Fig. 5-c2), but it should also be low enough to allow the later aggregation of polyhedra (Fig. 5-d3) and the subsequent sprouting from the $\{0001\}_{Ni}$ sites to form branches (Fig. 5-d4 → d5). Because the promoting ligands or etching ligands can change the monomer concentration [*m*] to potentially shift the growth mode between the nascent, 1D, and 2D growths, adjusting the concentration of neutral ligands can achieve the optimal ligand coverage without altering [*m*]. As a result, when a neutral ligand, *e.g.*, TDD, competes with the promoting ligands, *i.e.*, DDA or OAm, the interaction between $-NH_2$ and positively charged Ni atoms on the core's surface is weakened to partially relieve the constraint, lower the deposition barrier, encourage the once kinetically-hindered $\{0001\}_{Ni}$ growth, and eventually, grow the polyhedral aggregates into 3D urchins. To

verify this, we replaced DDA with TDD in a synthesis of polyhedral aggregates, and the resultant NBCs shifted to urchins as expected (Fig. 1 <9, J↔N, LS>).

Number of branches. The number of branches on the urchins and dandelions can be tuned as well. During the branching of NBCs, the Ni core branched from the surface protrusions, whereas OA at a higher concentration can etch down the least stable regions with the highest energy, so it may etch away some protrusions on the core to tune the number of branches in the resultant NBCs. To confirm this, when the amount of OA was increased from 7.93 mmol to 9.52 mmol, the number of branches on the dandelions was significantly reduced (Fig. 1 <24, W→T, EL>). If the amount of OA was further increased to 11.89 mmol, dandelions with even less branches were produced (Fig. 1 <23, T→P, EL>).

Plate formation. The development of 2D sub-structures in either dendrites or dandelions can create another level of hierarchy. A slow heating rate widens the nucleation window, consumes more monomers, and decreases μ_m below $\mu_{\{0001\}_{Ni}}$ to thermodynamically disable the 1D growth and promote the 2D growth. For the polyhedral aggregates, lowering the heating rate from ~5.26 °C min^{-1} to ~3.42 °C min^{-1} induced the stub formation over the surface as expected (Fig. 1 <11, K→J, HR>; note that the arrow points from the lower HR to the higher HR). For the urchins, a similar adjustment lead to the formation of platelets on the branches (Fig. 1 <25, W→V, HR>).

By attempting to connect the adjustment of the synthesis parameters to the morphological evolution *via* the formation mechanisms, these guidelines, hopefully, would operate analogously in other settings of solution-phase synthesis, and allow other branched nanostructures to be designed and synthesized with enhanced tunability.

Conclusions

Here we have presented a study of branching phenomena in solution-phase synthesis in depth and with precision. Twenty-four NBCs, in the morphologies of dots, core@shell dots, shells, clusters, polyhedra, platelets, dendrites, urchins, and dandelions, were synthesized (Fig. 1 and S1†) and characterized in detail (Fig. 2 and 3). The key synthesis parameters were identified, *e.g.*, heating rate, ligand concentration, and solvent volume, out of a myriad of convoluted parameters. Then a palette of classical or non-classical growth models, *i.e.*, nucleation, nascent growth, 1D growth, 2D growth, 3D reconstruction, aggregation, and carburization (Fig. 5), was defined and integrated to deconvolute the formation mechanism of each NBC. Eventually, some guidelines for tuning the branched morphologies were extracted to provide an alternative to time- and cost-intensive trials of *ad hoc* parameter adjustments without *a priori* knowledge of the growth behavior, *i.e.*, the particle size can be tuned *via* the solvent volume, and the number of branches can be manipulated with an etchant.

This work demonstrated a systematic approach to integrating the growth models as units to effectively deconvolute the formation mechanisms of complex nanostructures and improve the tunability of the syntheses of complex branched nanostructures, which should benefit the conception, development, and improvement of many other branched nanomaterials with desired biological, chemical, and physical properties for a broad range of applications in immunology,[6] catalysis,[3] energy storage,[7] and optics.[8,9] Hopefully, the better syntheses, improved properties, and broader applications of artificial branched nanostructures can in return deepen our understanding of natural branching phenomena and incentivize us to further study and benefit from nature.

Data availability

Essential data are provided in the main text and the ESI.† Additional data are available from the authors upon reasonable request.

Author contributions

M. S. and L. Q. conceived the idea and wrote up the draft. L. Q., F. Z., and W. Z. conducted most of the experiments. Y. C., X. X., Y. X., S. H., and M. J. helped with writing and data interpretation. J. L., Z. X., Y. L., and C. L. helped with some of the experiments. L. Q., G. G., Y. H., and Y. C. acquired the electron microscopy images. S. H., M. J., and M. S. provided the funding support. All of the authors contributed to the manuscript.

Conflicts of interest

The authors declare no competing financial interest.

Acknowledgements

We dedicate this paper to the late Dr Edward P. Furlani, an insightful theoretician and a sincere friend. L. Q. and S. H. would like to acknowledge support from the Petrochemical Research Institute. M. R. J. would like to thank the Robert A. Welch Foundation (Grant No. C-1954), the David and Lucile Packard Foundation (Grant No. 2018-68049), and Rice University for financial support. M. T. S. acknowledges support from the New York State Center of Excellence in Materials Informatics and the U.S. National Science Foundation (Grant No. CBET-1804996). The authors acknowledge the use of the Electron Microscopy Center (EMC) at Rice University.

References

1 K. G. Libbrecht, *Annu. Rev. Mater. Res.*, 2017, **47**, 271–295.
2 A. R. Poerwoprajitno, L. Gloag, J. Watt, S. Cychy, S. Cheong, P. V. Kumar, T. M. Benedetti, C. Deng, K.-H. Wu, C. E. Marjo, D. L. Huber, M. Muhler, J. J. Gooding, W. Schuhmann, D.-W. Wang and R. D. Tilley, *Angew. Chem., Int. Ed.*, 2020, **59**, 15487–15491.
3 J. Li, R. Wei, X. Wang, Y. Zuo, X. Han, J. Arbiol, J. Llorca, Y. Yang, A. Cabot and C. Cui, *Angew. Chem., Int. Ed.*, 2020, 20826–20830.
4 B. D. Clark, M. Lou, P. Nordlander and N. J. Halas, *Nano Lett.*, 2020, **20**, 6644–6650.

5 B. Lim, M. Jiang, P. H. Camargo, E. C. Cho, J. Tao, X. Lu, Y. Zhu and Y. Xia, *Science*, 2009, **324**, 1302–1305.
6 J. Wang, H.-J. Chen, T. Hang, Y. Yu, G. Liu, G. He, S. Xiao, B.-r. Yang, C. Yang, F. Liu, J. Tao, M. X. Wu and X. Xie, *Nat. Nanotechnol.*, 2018, **13**, 1078–1086.
7 Z. Chen, P.-C. Hsu, J. Lopez, Y. Li, J. W. To, N. Liu, C. Wang, S. C. Andrews, J. Liu, Y. Cui and Z. Bao, *Nat. Energy*, 2016, **1**, 15009.
8 D. G. Montjoy, J. H. Bahng, A. Eskafi, H. Hou and N. A. Kotov, *J. Am. Chem. Soc.*, 2018, **140**, 7835–7845.
9 S. R. Kirchner, M.-N. Su, J. H. Bahng, D. G. Montjoy, W.-S. Chang, N. Kotov and S. Link, *J. Phys. Chem. C*, 2018, **122**, 12015–12021.
10 M. V. Kovalenko, L. Manna, A. Cabot, Z. Hens, D. V. Talapin, C. R. Kagan, V. I. Klimov, A. L. Rogach, P. Reiss, D. J. Milliron, P. Guyot-Sionnnest, G. Konstantatos, W. J. Parak, T. Hyeon, B. A. Korgel, C. B. Murray and W. Heiss, *ACS Nano*, 2015, **9**, 1012–1057.
11 X. Cui, P. Xiao, J. Wang, M. Zhou, W. Guo, Y. Yang, Y. He, Z. Wang, Y. Yang, Y. Zhang and Z. Lin, *Angew. Chem., Int. Ed.*, 2017, **56**, 4488–4493.
12 K. Zhao, T. Qian, X. Bai, M. Feng, H. Gao, T. Xia, Z. Wang and H. Guo, *J. Phys. D: Appl. Phys.*, 2022, 344001.
13 X. Lv, Z. Fang, Y. Sun, Y. Yang, X. Wang, Y. Chen, Y. Qin, N. Li, C. Li and J. Xu, *J. Alloys Compd.*, 2023, **932**, 167712.
14 C. Bi, Y. Song, H. Zhao and G. Liu, *RSC Adv.*, 2022, **12**, 19571–19578.
15 A. Alinezhad, L. Gloag, T. M. Benedetti, S. Cheong, R. F. Webster, M. Roelsgaard, B. B. Iversen, W. Schuhmann, J. J. Gooding and R. D. Tilley, *J. Am. Chem. Soc.*, 2019, **141**, 16202–16207.
16 L. Qiao, W. Zhao, Y. Qin and M. T. Swihart, *Angew. Chem., Int. Ed.*, 2016, **55**, 8023–8026.
17 M. F. Sarac, W.-C. Wu and J. B. Tracy, *Chem. Mater.*, 2014, **26**, 3057–3064.
18 W. Zhou, K. Zheng, L. He, R. Wang, L. Guo, C. Chen, X. Han and Z. Zhang, *Nano Lett.*, 2008, **8**, 1147–1152.
19 V. K. LaMer and R. H. Dinegar, *J. Am. Chem. Soc.*, 1950, **72**, 4847–4854.
20 E. J. Popczun, J. R. McKone, C. G. Read, A. J. Biacchi, A. M. Wiltrout, N. S. Lewis and R. E. Schaak, *J. Am. Chem. Soc.*, 2013, **135**, 9267–9270.
21 L. M. Moreau, D.-H. Ha, H. Zhang, R. Hovden, D. A. Muller and R. D. Robinson, *Chem. Mater.*, 2013, **25**, 2394–2403.
22 Y. Song, Y. Yang, C. J. Medforth, E. Pereira, A. K. Singh, H. Xu, Y. Jiang, C. J. Brinker, F. van Swol and J. A. Shelnutt, *J. Am. Chem. Soc.*, 2004, **126**, 635–645.
23 L. He, *J. Magn. Magn. Mater.*, 2010, **322**, 1991–1993.
24 J. M. Rhodes, C. A. Jones, L. B. Thal and J. E. Macdonald, *Chem. Mater.*, 2017, **29**, 8521–8530.
25 J. Muro-Cruces, A. G. Roca, A. López-Ortega, E. Fantechi, D. del-Pozo-Bueno, S. Estradé, F. Peiró, B. Sepúlveda, F. Pineider, C. Sangregorio and J. Nogues, *ACS Nano*, 2019, **13**, 7716–7728.
26 S. Carenco, S. Labouille, S. Bouchonnet, C. Boissiere, X. F. Le Goff, C. Sanchez and N. Mezailles, *Chem.–Eur. J.*, 2012, **18**, 14165–14173.
27 J. Li, H. Wang, L. Lin, Q. Fang and X. Peng, *J. Am. Chem. Soc.*, 2018, **140**, 5474–5484.
28 M. R. Hauwiller, X. Ye, M. R. Jones, C. M. Chan, J. J. Calvin, M. F. Crook, H. Zheng and A. P. Alivisatos, *ACS Nano*, 2020, **14**, 10239–10250.
29 A. E. Henkes, Y. Vasquez and R. E. Schaak, *J. Am. Chem. Soc.*, 2007, **129**, 1896–1897.
30 L. M. Moreau, D.-H. Ha, C. R. Bealing, H. Zhang, R. G. Hennig and R. D. Robinson, *Nano Lett.*, 2012, **12**, 4530–4539.
31 K. Momma and F. Izumi, *J. Appl. Crystallogr.*, 2011, **44**, 1272–1276.
32 V. N. Richards, S. P. Shields and W. E. Buhro, *Chem. Mater.*, 2011, **23**, 137–144.
33 I. V. Markov, *Crystal growth for beginners: fundamentals of nucleation, crystal growth and epitaxy*, World scientific, 2016.
34 Z. A. Peng and X. Peng, *J. Am. Chem. Soc.*, 2001, **123**, 1389–1395.
35 Z. L. Schaefer, K. M. Weeber, R. Misra, P. Schiffer and R. E. Schaak, *Chem. Mater.*, 2011, **23**, 2475–2480.
36 X. Xue, J. Wang and E. P. Furlani, *ACS Appl. Mater. Interfaces*, 2015, **7**, 22515–22524.
37 A. Riedinger, F. D. Ott, A. Mule, S. Mazzotti, P. N. Knusel, S. J. P. Kress, F. Prins, S. C. Erwin and D. J. Norris, *Nat. Mater.*, 2017, **16**, 743–748.
38 J. E. Millstone, S. J. Hurst, G. S. Métraux, J. I. Cutler and C. A. Mirkin, *Small*, 2009, **5**, 646–664.
39 T. Witten Jr and L. M. Sander, *Phys. Rev. Lett.*, 1981, **47**, 1400.
40 X. Yin, J. Shi, X. Niu, H. Huang and X. Wang, *Nano Lett.*, 2015, **15**, 7766–7772.
41 Y. Xu, N. G. Petrik, R. S. Smith, B. D. Kay and G. A. Kimmel, *Proc. Natl. Acad. Sci. U. S. A.*, 2016, **113**, 14921–14925.
42 Z. A. Peng and X. Peng, *J. Am. Chem. Soc.*, 2002, **124**, 3343–3353.
43 X. Yin and X. Wang, *Nano Lett.*, 2016, **16**, 7078–7084.
44 W. Ostwald, *Z. Phys. Chem.*, 1897, **22**, 289–330.
45 R. W. Emerson, *The Essential Writings of Ralph Waldo Emerson*, Modern Library Classics, 2000.